Chemistry Europe
European Chemical Societies Publishing

WILEY VCH

Excellence in Chemistry Research

Announcing our new flagship journal

- Gold Open Access
- Publishing charges waived
- Preprints welcome
- Edited by active scientists

Meet the Editors of *ChemistryEurope*

Luisa De Cola
Università degli Studi di Milano Statale, Italy

Ive Hermans
University of Wisconsin-Madison, USA

Ken Tanaka
Tokyo Institute of Technology, Japan

ChemSusChem

Research Article
doi.org/10.1002/cssc.202300399

Chemistry Europe
European Chemical Societies Publishing

www.chemsuschem.org

Hexavalent Ions Insertion in Garnet $Li_7La_3Zr_2O_{12}$ Toward a Low Temperature Densification Reaction

Daniele Campanella,[a, b] Wen Zhu,[a] Gabriel Girard,[a] Sylvio Savoie,[a] Shirin Kaboli,[a] Zimin Feng,[a] Abdelbast Guerfi,[a] Martina Romio,[c] Palanivel Molaiyan,[c] Daniel Bélanger,[b] and Andrea Paolella*[c, d]

Nowadays, solid electrolytes are considered the main alternative to conventional liquid electrolytes in lithium batteries. The fabrication of these materials is however limited by the strict synthesis conditions, requiring high temperatures which can negatively impact the final performances. Here, it is shown that a modification of garnet-based $Li_7La_3Zr_2O_{12}$ (LLZO) and the incorporation of tellurium can accelerate the synthesis process by lowering the formation temperature of cubic LLZO at temperatures below 700 °C. Optimized synthesis at 750 °C showed a decrease in particle size and cell parameter for samples with higher amounts of Te and the evaluation of electrochemical performances reported for LLZO Te0.25 a value of ionic conductivity of $5{,}15\times10^{-5}$ S cm^{-1} after hot-pressing at 700 °C, two orders of magnitude higher than commercial Al-LLZO undergoing the same working conditions, and the highest value at this densification temperature. Partial segregation of Te-rich phases occurs for high-temperature densification. Our study shows the advantages of Te insertion on the sintering process of LLZO garnet and demonstrates the achievement of highly conductive LLZO with a low-temperature treatment.

Introduction

The topic of energy storage has critical importance in modern society. The capillary diffusion of portable electronic devices and the development in the field of electric vehicles (EVs) are forcing us to face up to increasing energy demand. Modern technologies moving past the traditional lithium-ion battery concept,[1] such as Li-air or Li–S batteries, are steadily gaining traction due to their remarkable properties in terms of energy and power density.[2,3] Still, Li-metal batteries sustain the problem of lithium dendrites,[4] which can lead to short-circuiting of the battery and cause severe safety risks in the presence of flammable liquid electrolytes. In Li-air and Li–S systems, the phenomenon of electrolyte decomposition is a significant issue that seriously hinders the global performances and efficiencies of the system.[5,6] Because of these safety hitches, strong efforts have been made for the development of all-solid-state Li-ion batteries (ASSLIBs),[7,8] replacing conventional graphite-based anodes and flammable electrolytes with Li-metal anodes and solid-state electrolytes.[8] Among the families of materials investigated for this purpose, we can find polymers (PEO-LiTFSI),[9] ceramics (e.g., garnets[10], perovskites,[11] NaSICON,[12,13] sulfides[14] and halides[15,16]) and hybrids (ceramic-polymer composites).[17,18] A good solid electrolyte should meet several requirements: a wide stability window against Li metal and high-voltage cathodes,[19,20] a high room temperature ionic conductivity ($>10^{-3}$ S cm^{-1}) with low electronic conductivity,[21] a good chemical and thermal stability, and good mechanical properties.[22] Garnet-based solid-state electrolytes are one of the most promising solutions,[23–25] due to their aptness in accommodating excess Li,[26] their remarkably high ionic conductivities,[27–30] reaching 10^{-4} S cm^{-1}, and their stability towards metallic Li, air, and moisture.[27–29] Moreover, their wide voltage stability window (up to 6 V) renders them compatible with high-voltage cathodes.[28,31] $Li_7La_3Zr_2O_{12}$ (LLZO) has attracted strong interest because of its high Li^+ ions content and occupancy of octahedral sites, which could increment Li-ion transport in the structure.[30] LLZO presents two different crystal polymorphs: 1) an $I4_1/acd$ tetragonal phase and 2) an $Ia\bar{3}d$ cubic phase. The two phases have the same stoichiometry and framework structure but a different distribution of Li^+ ions, which has a strong impact on the ionic diffusion mechanism and electrochemical performance.[32] The material undergoes a tetragonal-to-cubic phase transition at high temperatures[33] due to lithium loss,[34] and the former exhibits a conductivity ($\approx10^{-6}$ S cm^{-1})[35] about two orders of magnitude lower than the latter ($\approx10^{-4}$ S cm^{-1}).[36] Undoped LLZO tends to crystallize in the tetragonal phase at room temperature,[35] which has been found to be the most thermodynamically stable phase and is generally obtained via solid-state reactions at $T \approx 1000$ °C,

[a] D. Campanella, W. Zhu, G. Girard, S. Savoie, S. Kaboli, Dr. Z. Feng, Dr. A. Guerfi
Centre d'Excellence en Électrification des Transports et Stockage d'Energie (CEETSE)
Hydro-Québec, Varennes, Québec J3X 1S1 (Canada)
[b] D. Campanella, Prof. D. Bélanger
Département de Chimie
Université du Québec à Montréal (UQAM)
2101 Rue Jeanne-Mance, Montréal, Québec, H3C 3P8 (Canada)
[c] M. Romio, P. Molaiyan, Dr. A. Paolella
Austrian Institute of Technology (AIT), Battery Tecnologies
Giefinggasse 2, 1210 Wien (Austria)
E-mail: andrea.paolella@ait.ac.at
[d] Dr. A. Paolella
Department of Inorganic Chemistry-Functional Materials
University of Vienna
Währinger Straße 42, 1090 Vienna (Austria)

whereas for the production of the cubic form with standard ceramic process higher temperatures (above 1200 °C) are required. Ionic substitution has been proven to help decrease the sintering temperature below 1100 °C and stabilize the cubic phase at room temperature.[37] The cubic phase is typically obtained with the introduction of doping elements alongside the usual LLZO precursors. Partial replacement of Li with supervalent cations like Al,[38] Ga[39], and Y[40] has been observed to increment the concentration of Li^+ vacancies in the structure,[41] hence allowing to obtain a highly conductive cubic LLZO. Substitution of Zr(IV) with pentavalent cations, such as Ta,[42] Nb[43] or Bi,[44,45] is another possible solution for stabilising the cubic structure and improve Li^+ ions transport. Li et al.[46] showed that a partial doping with W(VI) on the Zr site has a positive effect on the densification of the material, resulting in high density and an improved conductivity. Incorporating high-entropy cations within the structural scaffold can positively influence the distribution of site energies and, consequently, the percolating transport of charge carriers, hence leading to a global improvement of the conductive properties.[47] Ions such as Hf, Te, and rare earth elements may enhance the ionic conductivity of solid electrolytes of several orders of magnitude compared with the undoped materials.[47,48] Te-doped LLZO was successfully prepared via solid state reaction[49] and presented a bulk conductivity of about 1,02 $mS\,cm^{-1}$ at room temperature (RT) after high temperature sintering, whilst the simultaneous introduction of Te and Al stabilized the cubic phase and lowered the activation energy, at the expense of a lower conductivity (4×10^{-4} $S\,cm^{-1}$).[50]

The purpose of this work is to investigate the effects of hot-pressing on Te-doped LLZO about its structural and electrochemical properties. Hot-pressing has been often employed as a technique to improve the annealing process of ceramic materials and involves the concurrent application of uniaxial pressure and heat.[51,52] This allows a lower-temperature densification and shorter processing times and eventually leads to benefits such as a reduced loss of lithium, with positive effects on the ionic conductivity. Here, we report a series of $Li_{7-2x}La_3Zr_{2-x}Te_xO_{12}$ ($x=0.1$, 0.25, 0.375, 0.5) compositions. Several techniques were employed to determine the influence of doping on the synthesis and electrochemical performances of the materials.

Experimental Section

A series of Te-doped lithium garnets with compositions $Li_{7-2x}La_3Zr_{2-x}Te_xO_{12}$ ($x=0.1$, 0.25, 0.375, 0.5) were synthesised via conventional solid-state reaction. The precursors LiOH (Sigma Aldrich, anhydrous powder, purity 99.9% trace metals basis), La_2O_3 (Sigma Aldrich, powder, purity 99.99% trace metals basis), ZrO_2 (Sigma Aldrich, powder, 5 μm, purity 99% trace metals basis) and TeO_2 (Sigma Aldrich, powder, purity ≥99%) were mixed and ground using a Retsch PM-100 planetary ball mill with 16 mm zirconia balls in a zirconia coated jar. A 10 wt% excess of LiOH was added to the mixture to make up for the loss of lithium during the synthesis process. The materials were ground for 6 h at 400 rpm and calcined at 750 °C for 6 h. The resulting powder was subsequently hot-pressed under flowing Ar atmosphere. To avoid pellet gluing, the annealing took place in a 16 mm Si_3N_4 die with WC pistons, and carbon paper films were applied on both sides of the powder, to ensure a conductive coating for the pellet. The hot-press treatment was carried out at temperatures 600 °C, 650 °C and 700 °C for 1 h under a pressure of 2 tons, with a temperature increment of 20 °C per minute during the heating step. The LLZO phase formation was investigated via in situ X-ray diffraction. The analysis took place in a Bruker D8 advance diffractometer equipped with an Anton Paar DHS 1100 domed hot stage, and it was performed on mixtures of LLZO precursors with and without Te ($x=0.25$). The samples were heated to 855 °C at a rate of 30 °C min^{-1} and held at the temperature for 3 h under air flow. The XRD spectra were collected every 6 min. The calcined powders were characterised by X-ray diffraction in a Rigaku Miniflex600 diffractometer at RT in a 2θ range from 10° to 100° with a step of 0,02° to determine the final phase of the materials. The surface morphology of the sintered powders was investigated by scanning electron microscopy (SEM) using a Hitachi FlexSEM1000 electronic microscope. SEM cross-section surfaces were set up with the help of an Ar Ion Milling IM4000 Plus (Hitachi, Japan) with an ion beam energy of 6 kV at a 30° rotation for 4 h and subsequently analyzed using a Lyra 3 (TESCAN) SEM equipped with an Oxford Instruments Energy-Dispersive Spectroscopy (EDS) detector. Electrochemical impedance spectroscopy (EIS) measures were performed to measure ionic conductivity, using a BioLogic VMP-300 potentiostat with frequency ranging from 1 Hz to $7x10^6$ Hz, in a temperature interval between 25 °C and 80 °C for all samples.

Results and Discussion

We explored the evolution of LLZO phase following the incorporation of tellurium using in situ XRD to comprehend the reactivity of the synthesis precursors as shown in Figure 1a. The tellurium-free sample (black patterns) shows the evolution of synthesis intermediates $La_2Zr_2O_7$ and Li_2ZrO_3 in the temperature interval between 555 and 755 °C, following the reactions $La_2O_3 + 2ZrO_2 \rightarrow La_2Zr_2O_7$ and $Li_2O + ZrO_2 \rightarrow Li_2ZrO_3$. The formation of the LLZO phase is first observed above 755 °C but the relative intensity of the peaks remains low until reaching higher temperatures (>850 °C). The formation mechanism is related to the reaction between the intermediates previously formed (possibly following the equation $La_2Zr_2O_7 + Li_2ZrO_3 + Li_2O + La_2O_3 \rightarrow c\text{-}Li_7La_3Zr_2O_{12}$). The XRD patterns display the peak of an unidentified phase around 22° during the heating steps, which suddenly disappears upon reaching the hold temperature of 855 °C. On the other hand, the mixture of precursors containing Te (red patterns) exhibits a different behaviour, manifesting the absence of the mixed phases during the heating segment. The evolution of the cubic LLZO phase follows directly from the synthesis precursors in the starting mix and first presence of its presence is observed at temperatures between 555 and 755 °C. Cubic LLZO becomes a major phase in the mix above 755 °C and the peaks related to the remaining unreacted phases of La_2O_3 steadily fade out during the high temperature hold, leaving an almost pure LLZO phase. The reaction supposedly undergoes a direct mechanism according to the equation $1.5La_2O_3 + 2ZrO_2 + 3.5Li_2O \rightarrow c\text{-}Li_7La_3Zr_2O_{12}$. During the 3 h hold time at 855 °C, the diffraction patterns for both samples show a main presence of the LLZO phase. The

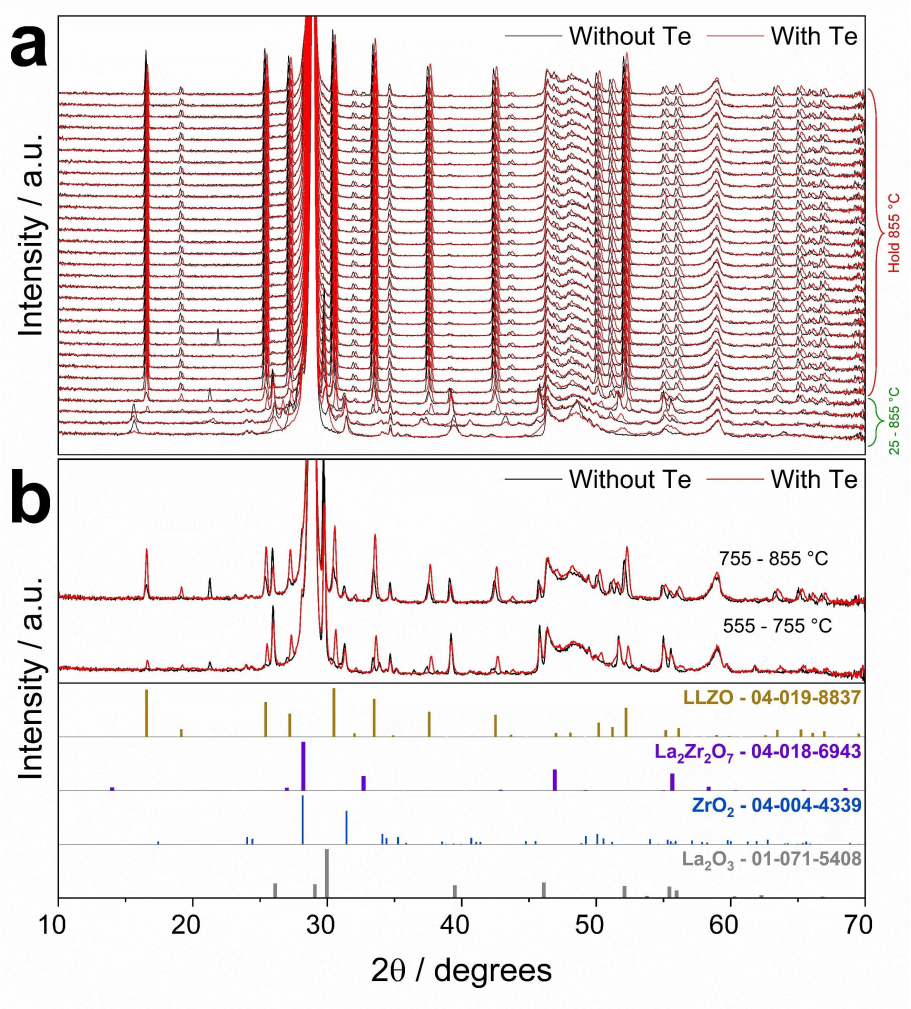

Figure 1. a) Compared evolution of in situ XRD patterns for precursors mix with and without Te addition during the heating process of LLZO precursors in a range of temperature from 25 °C to 855 °C and during the hold step. b) Highlighted XRD patterns during the heating step (555-755 °C and 755–855 °C) compared with the reference patterns for LLZO and synthesis intermediates.

highlighted patterns in Figure 1b, show more visibly the relative intensity of the LLZO peaks in the heating step, confirming the more rapid evolution of the cubic product in the sample with Te incorporation. This result confirms the influence of tellurium in lowering the temperature formation of LLZO.

To observe more in detail the direct effects of Te incorporation, powders with different Tellurium amounts were prepared by increasing Te content $Li_{7-2x}La_3Zr_{2-x}Te_xO_{12}$ ($x=0.1$, 0.25, 0.375, 0.5): the different compositions were synthesised with a single annealing step at 750 °C for 6 h, following a process already reported in literature.[49] An undoped sample was prepared following the same procedure as reference. The compared X-ray diffraction patterns for the resulting powders are reported in Figure 2a. The pattern for the undoped sample displays a singular behaviour, showing the characteristic peaks of a tetragonal LLZO phase, such as the bicuspid peak at $2\theta=$ 19.5°. This may indicate that the absence of tellurium in the precursor mix hampers the formation of the cubic phase for a low temperature synthesis process. This aspect is further confirmed by the XRD patterns for the different Te-doped compositions, all of which manifest the characteristic peaks of a cubic phase, without showing the typical peak splitting of the tetragonal phase ($2\theta=19.5°$ and 30°). Such display points out the proper crystallization of the expected cubic phase even for relatively low incorporation of tellurium in the structure. The samples with higher Te content ($x=0.25$ and higher) revealed some identifying peaks corresponding to a secondary phase of lithium tellurate (Li_6TeO_6, R$\bar{3}$, ICDD 00-022-0418). In particular, the XRD patterns for $x=0.375$ and $x=0.5$ manifest intense peaks at $2\theta=21.1°$, 33.8° and 50.9°. This could indicate a partial phase segregation in presence of exceedingly high tellurium content in the material, which can depend on the nature of the synthesis process itself as observed by the absence of corresponding peaks in the in-situ patterns. Moreover, the XRD pattern for $x=0.5$ shows an additional minor peak at $2\theta=34.9°$ indicating the presence of La_2O_3 impurities. The morphology manifested by the Te-doped powders (Figures 2b–e) has the typical rounded potato shape of LLZO particles and the images

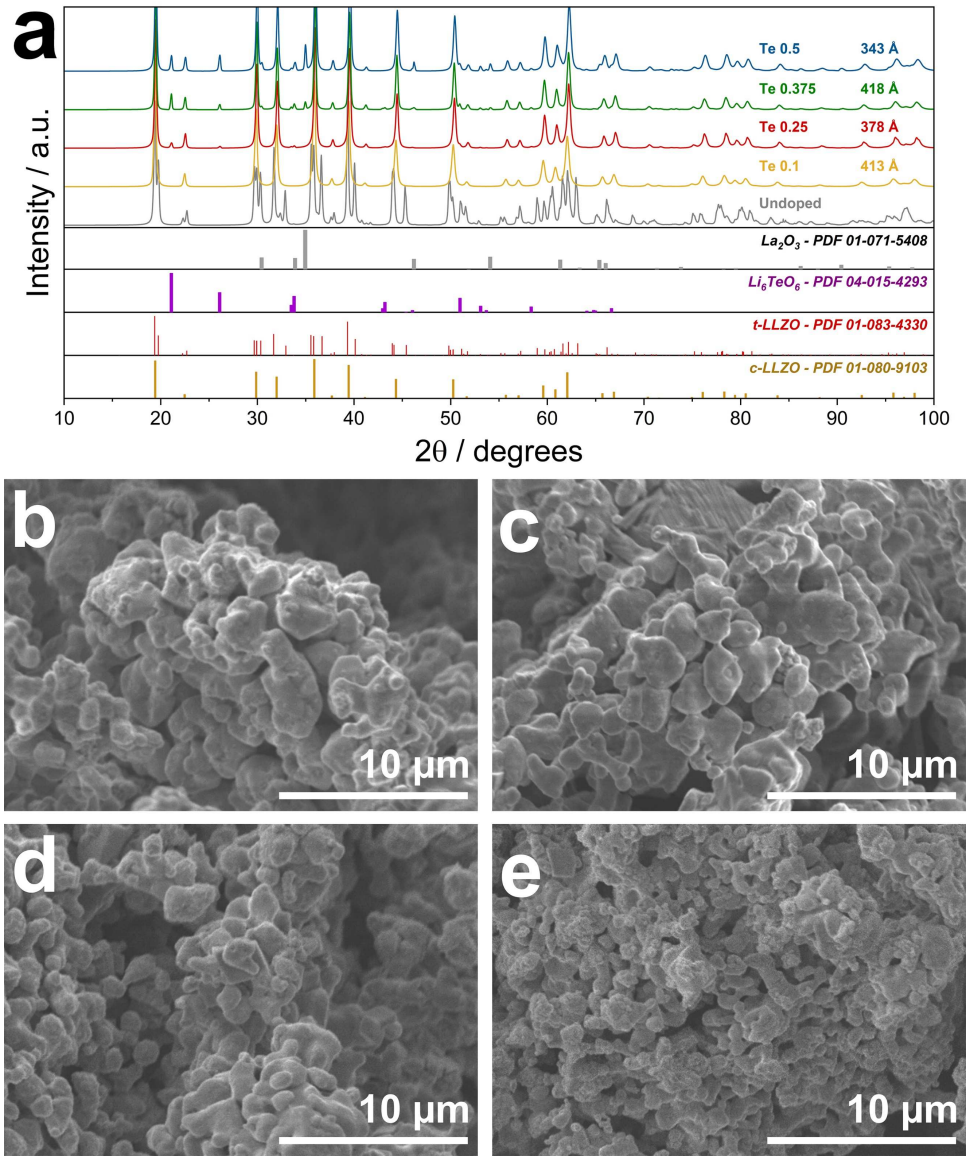

Figure 2. a) XRD patterns for powders of with different Te content, annealed at 750 °C for 6 h, compared with the PDF cards. The image reports the value of the average crystallite size for the Te-doped samples; b–e) SEM images for the synthesized powders with different carbon content: b) Te 0.1, c) Te 0.25, d) Te 0.375 and e) Te 0.5.

seem to display a slight but visible diminution in the surface particle size for the specimens with higher Te presence. A similar behaviour has recently been observed by our group with the incorporation of graphite in LLZO.[53]

The calculated lattice parameters of all $Li_{7-2x}La_3Zr_{2-x}Te_xO_{12}$ compositions are found in Table 1. As reported, the materials display a continuous decrease in the value of cell parameters, going from 12.9921 Å for $x=0.1$ to 12.9585 Å for $x=0.5$, in accordance with previous results found in literature.[49,54] A possible reason for this phenomenon may be found in the diminution in Li content along with the concurrent substitution of large Zr^{4+} cations ($r=0.72$ Å) with much smaller Te^{6+} ions ($r=0.56$ Å). The results of the XRD analysis therefore confirms the successful attainment of a cubic LLZO after a low temperature sintering for all stoichiometries due to the partial introduction of Te in the garnet structure. The graph reports the values of the average crystallite size, and we can observe a general trend showing a decrease in size with the increment of

Table 1. Evolution of the α cell parameter for the Te-doped LLZO samples.

Calculated lattice parameters	
x_{Te}	α [Å]
0.1	12.9921
0.25	12.9822
0.375	12.9672
0.5	12.9585

Te content, with the significant exception of Te0.375 which shows the highest value of 418 Å.

To better understand the influence of tellurium on cubic structure stability of LLZO we performed modelling experiments. More in details, one can heuristically infer the impact from doping on the change of configurational entropy, and henceforth on the phase transition. Consider the pristine LLZO, there are 24 d-sites, 48 g-sites and 96 h-sites for 56 Li ions in a unit cell. Nevertheless, it is almost impossible for more than one Li^+ ions to simultaneously occupy two or all the three adjacent h- and g-sites due to the strong Coulomb repulsion. Hence, the number of possible configurations should read [Eq. (1)]:

$$\Omega_{\text{pristine}} = \sum_{i=8}^{24} \binom{24}{i}\binom{48}{56-i} 3^{56-i} \approx 1.5696 \times 10^{34} \quad (1)$$

This gives an entropy of [Eq. (2)]:

$$S_{\text{pristine}} = k_B \log \Omega_{\text{pristine}} \approx 6.79 \text{ meV K}^{-1} \quad (2)$$

When LLZO is doped with higher valence elements, the number of Li ions in a unit cell is reduced. In our case (Figure 3) we have 48 Li ions in a unit cell. In this case, the number of possible configurations, and consequently the configurational entropy, increase [Eqs. (3) and (4)].

$$\Omega_{\text{doped}} = \sum_{i=0}^{24} \binom{24}{i}\binom{48}{48-i} 3^{48-i} \approx 1.3644 \times 10^{35} \quad (3)$$

$$S_{\text{doped}} = k_B \log \Omega_{\text{doped}} \approx 6.97 \text{ meV K}^{-1} \quad (4)$$

In the tetragonal phase, however, the Li^+ ions do not have partial occupancy in the pristine LLZO. Although doping could create some Li^+ vacancies, the hopping energy barrier of 0.4 eV in tetragonal phase effectively makes the hopping of Li^+ ions a rare event, therefore tetragonal phases are safely considered to have zero configurational entropy. Generally, a phase with higher entropy is preferred at higher temperatures while a phase with lower entropy appears at lower temperatures.

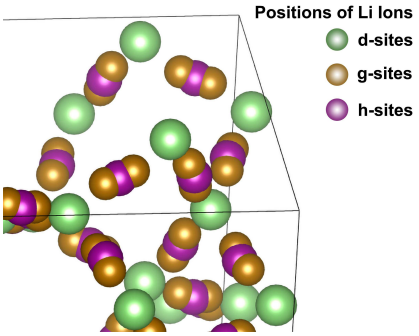

Figure 3. Distribution of Li ion sites in the cubic LLZO unit cell.

Although doped LLZO doesn't always have tetragonal phases, it is still interesting to observe that, since the difference in (configurational) entropy between doped cubic phase and doped tetragonal phase is larger than that between the two pristine phases, the phase transition temperature of cubic to tetragonal is expected to be lower than that of the pristine LLZO, aside from other factors. In this regard, doping LLZO is beneficial to keeping it in its highly conducting cubic phase. To electrochemically evaluate the effects of Te incorporation on the total ionic conductivity of the garnet, the different samples were hot-pressed at different temperatures (600, 650 and 700 °C) under a pressure of 56 MPa. EIS tests were subsequently performed into coin cells and the resulting pellets were sandwiched between stainless steel electrodes. The analyses took place in the temperature range from 20 to 80 °C and Figure 4a reports the resulting Nyquist plots collected at 20 °C for the pellets hot-pressed at 650 °C. The different spectra show an important difference in the values of resistance for the materials, represented by the amplitude of the depressed semicircle. Te0.1 exhibits values of resistance of 4,5 kΩ at room temperature, about twice as large than the values for the samples with higher Te content while the lower value is reported for Te0.25; a subsequent data fitting of the Nyquist plots permitted to derive of the values of ionic conductivity. The corresponding Arrhenius plots are reported in Figure 4b; in the graphs it can be observed a similar behaviour in the values of conductivity for all the different samples, for which an increase in the hot-pressing temperature is followed by an increment of the ionic conductivity. The Te0.1 sample is an exception: the conductivities at different annealing temperatures are similar and, surprisingly, slightly higher for the pellet densified at 650 °C ($1{,}76\times10^{-5}$ S cm^{-1}) compared to the one treated at 700 °C ($1{,}45\times10^{-5}$ S cm^{-1}). This may indicate that the incorporation of low amounts ($\leq$10 %) of Te in the structure does not have a significant impact on the final conductivity. On the other hand, the highest values are reported for the Te0.25 sample, showing a room temperature conductivity of $5{,}15\times10^{-5}$ S cm^{-1} for Te 0.25–700, about 1,5 times higher than that of Te0.25–600 ($2{,}95\times10^{-5}$ S cm^{-1}). In general, it can be observed that Te insertion can positively influence the stabilization of the cubic-LLZO phase during low temperature hot-pressing; to better understand the effects, a comparison between Te-LLZO and commercial samples of Al and Ta-doped LLZO, has been carried out. Te0.25 has been chosen for the comparison due to its overall better performance. The results are shown in Figure 4c, and we can see that the performance for Te-LLZO is much better than the ones for commercial LLZO treated at the same working conditions. Low temperature treatment doesn't help achieving good densification in commercial samples and this reflects in the average conductivity being astoundingly lower than that of Te-LLZO, about one order of magnitude lower for Ta-LLZO ($6{,}70\times10^{-6}$ vs. $5{,}15\times10^{-5}$ S cm^{-1} for samples densified at 700 °C) and two orders of magnitude for Al-LLZO ($3{,}05\times10^{-7}$ vs. $5{,}15\times10^{-5}$ S cm^{-1}). All conductivity values are reported in Table 2 and the results further confirm the major influence of Te incorporation on the electrochemical performances of LLZO solid electrolyte and its advantages in improving

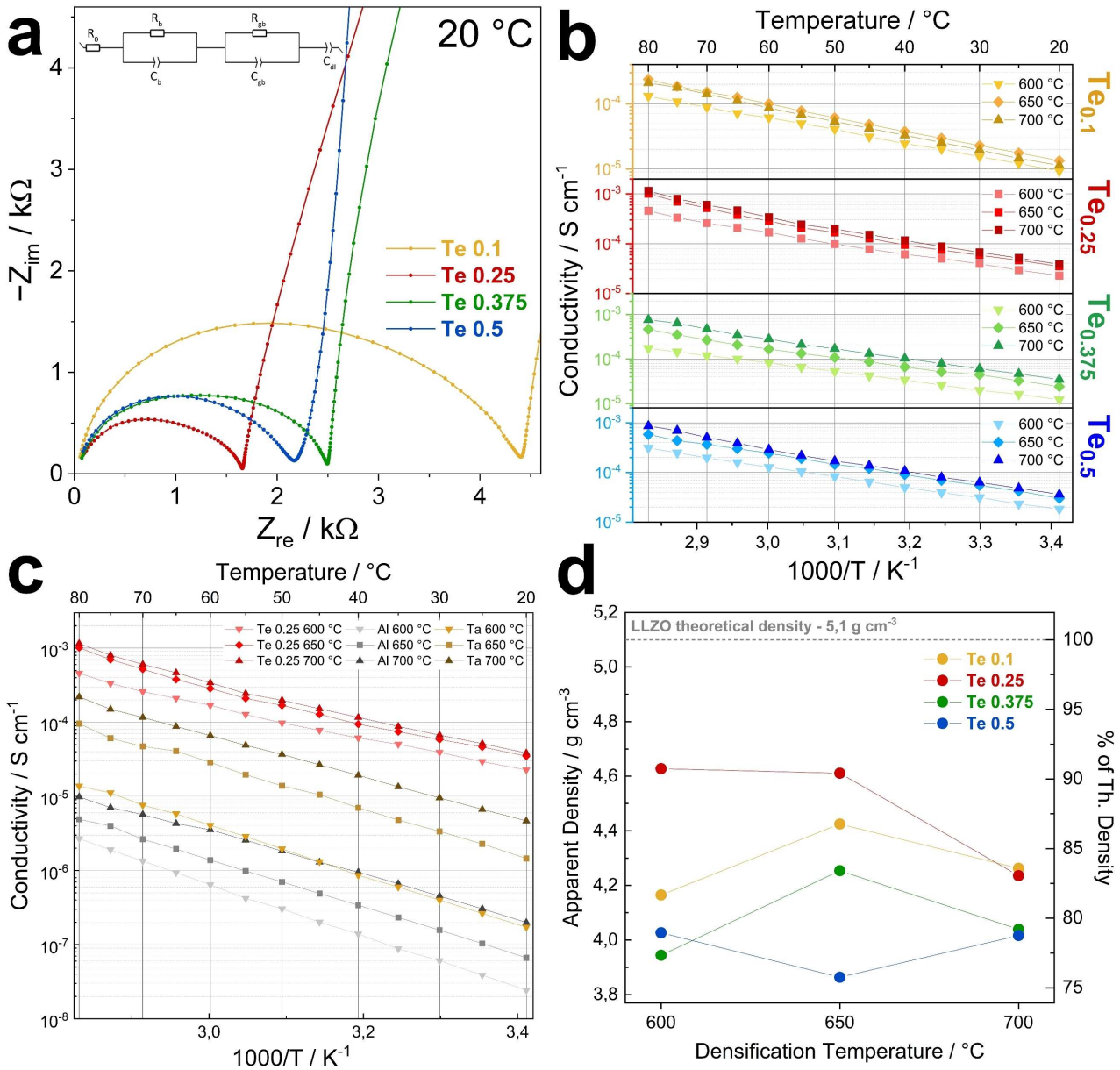

Figure 4. a) Nyquist plots of the impedance for different Te-doped LLZO densified at 650 °C samples measured at 20 °C. The image reports the equivalent circuit used for data fitting. b) Arrhenius plots of the total ionic conductivity of the different Te-doped LLZO samples densified at different temperatures in the temperature range from 20 to 80 °C. c) Compared Arrhenius plots of the total ionic conductivity of Te0.25 samples and commercial Al and Ta doped LLZO densified in the same working conditions. d) Graph of apparent density of Te-LLZO samples densified at different temperatures.

Table 2. Conductivity values at different temperatures of the different LLZO samples.

T [°C]	σ (25 °C) [S cm^{-1}] Te0.1	Te0.25	Te0.375	Te0.5	Al-LLZO	Ta-LLZO
600 °C	1,21x10^{-5}	2,95x10^{-5}	1,61x10^{-5}	2,33x10^{-5}	3,88x10^{-8}	2,64x10^{-7}
650 °C	1,76x10^{-5}	4,64x10^{-5}	3,27x10^{-5}	4,24x10^{-5}	1,04x10^{-7}	2,29x10^{-6}
700 °C	1,45x10^{-5}	5,15x10^{-5}	4,66x10^{-5}	4,83x10^{-5}	3,05x10^{-7}	6,70x10^{-6}

the material densification at lower temperatures. In Figure 4d the values of apparent density of the different Te-LLZO samples are reported. An irregular behaviour of the density values is observed, and the samples generally exhibit lower values of density after densification at 700 °C, compared to 650 °C, except for Te0.5. A precise evaluation of the effective values proves rather difficult because of the nature of the hot-pressing process itself: high temperature treatment in strict conditions

often causes partial loss of material and the sintering of the pellets is affected, leading to inaccurate density values. In the graph we can however observe the highest values of density associated with Te0.25 sample, exceeding 90% of the theoretical value (LLZO density = 5.1 g cm^{-3}), which reflect the better electrochemical performances of the specimen.

Figure 5a–c reports the SEM cross section images of Te0.25 pellets after hot-pressing along with the EDS mapping for the main elements. A more uniform distribution of the elements is observed for the sample densified at 600 °C (HP600), with the presence of small areas of Te segregation (Figure 5a). On the other hand, the elemental distribution for the pellets hot-pressed at higher temperatures display wide spots with a significantly higher presence of Te and a lower concentration of La and Zr, which may indicate a higher degree of segregation of Te-rich phases after high temperature treatment. Sample HP700 (Figure 5c) shows vast areas of Te segregation with almost absent presence of La and Zr, and these areas are reflected in the electron image showing large voids between the particles. The formation of separate phases abundant in Te may have a notable impact on the densification of the material. Figure 5d reports the XRD patterns of the powders of the different Te0.25 pellets after densification and the material manifests a similar pattern before and after hot-pressing. HP600

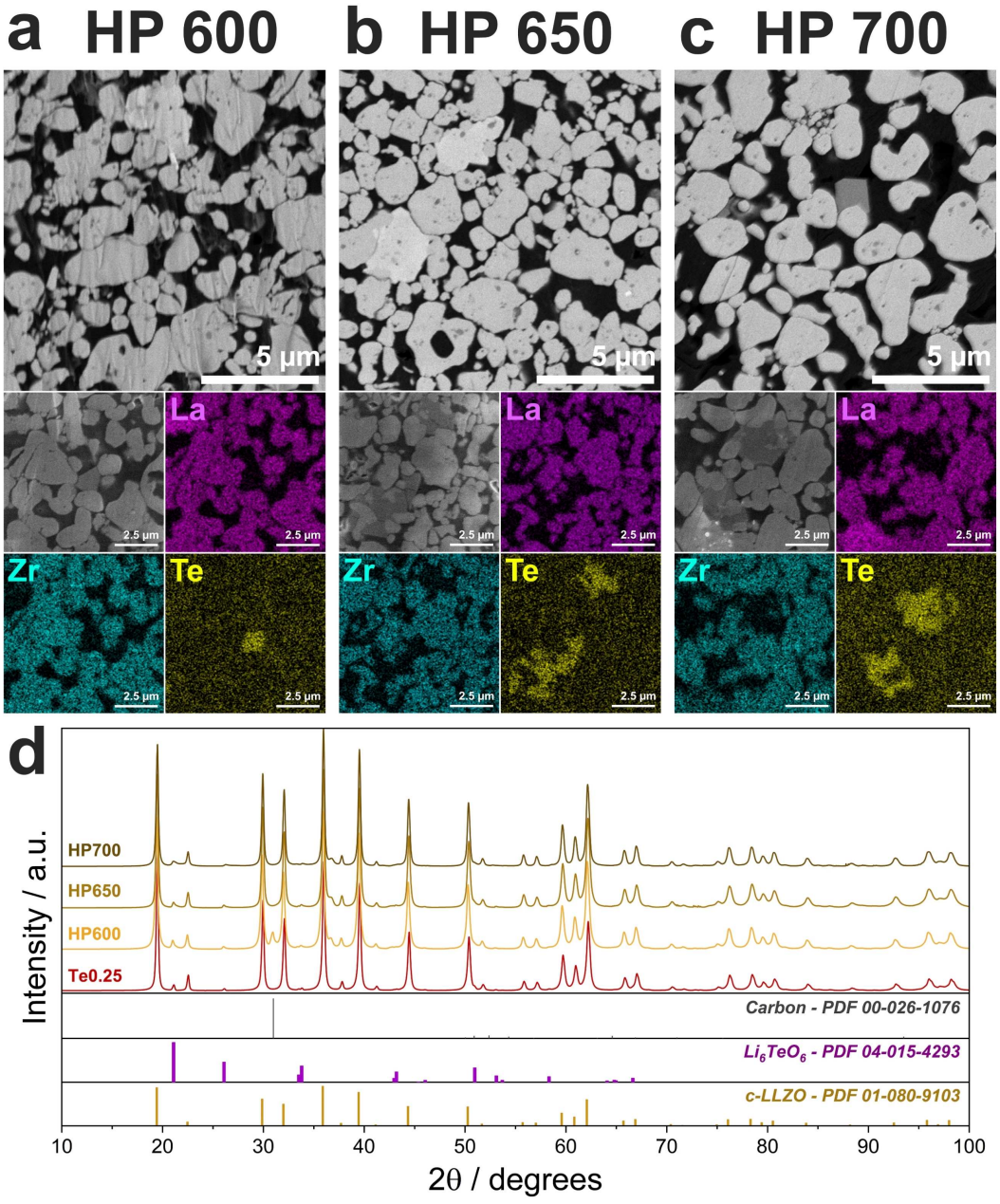

Figure 5. a–c) Cross section SEM images and EDS elemental mapping for La, Zr and Te of LLZO Te0.25 at different hot-pressing temperatures: a) 600 °C (HP600), b) 650 °C (HP650) and c) 700 °C (HP700). d) XRD patterns for the powders of hot-pressed LLZO Te0.25 pellets compared with the pristine powder before hot pressing.

shows an additional peak at about 31° indicating the presence of carbon, possibly due to small traces of the carbon conductor used for the annealing. The patterns show the absence of additional phases compared with the powder before hot-pressing, with the presence of the Te-rich secondary phase of Li_6TeO_6, which most likely constitutes the segregating phase observed in the EDS maps of Figures 5a–c. The formation of Li_6TeO_6 at the grains interphase is consistent with previous observations reported in literature for other dopants, such as aluminium or gallium.[55,56]

Conclusions

In this work we investigated the effects of tellurium insertion in the synthesis process of garnet $Li_7La_3Zr_2O_{12}$ (LLZO) prepared via solid-state reaction. Incorporation of Te affects the reaction mechanism of the electrolyte synthesis during the calcination, enabling the formation of cubic LLZO at lower temperatures. Even relatively low amounts of Te in the material have a positive impact in obtaining a cubic polymorph and tellurium incorporation helps stabilizing the structure and reducing the average particle size, possibly improving the densification of the ceramic electrolyte. Te-ions show a positive effect in the electrochemical properties of the material, as confirmed by electrochemical impedance spectroscopy. Te doped LLZO showed promising values of ionic conductivity after low-temperature hot-pressing, with the highest values of $5{,}15 \times 10^{-5}$ S cm^{-1} reported for Te0.25 densified at 700 °C. This value is reported as the highest value achieved at this densification temperature, more than two orders of magnitude higher than commercial Al-LLZO densified in the same working conditions. The present work reports a promising method to obtain highly conductive LLZO at lower temperatures and to improve the electrochemical properties of garnet solid electrolytes.

Acknowledgements

The research was funded by Hydro-Québec's Centre of Excellence in Transportation Electrification and Energy Storage, Varennes, Québec. D.C. and W.Z. thank Olivier Sioui-Latulippe of Polytechnique Montréal for his support in the in-situ analysis. D.C. thanks Dr. Kim Chisu of CEETSE (Canada) for her suggestions. A.P. thanks Prof. Karim Zaghib of Concordia University (Canada) and Dr. Hendrix Demers of CEETSE (Canada) for their useful suggestions. D.C. acknowledges the financial support of Mitacs.

Conflict of Interests

The authors declare no conflict of interest.

Data Availability Statement

The data that support the findings of this study are available from the corresponding author upon reasonable request.

Keywords: lithium batteries · solid electrolytes · tellurium ions · grain boundaries · stable structure

[1] B. Scrosati, J. Hassoun, Y.-K. Sun, *Energy Environ. Sci.* **2011**, *4*, 3287.
[2] M. Armand, J.-M. Tarascon, *Nature* **2008**, *451*, 652–657.
[3] A. Varzi, K. Thanner, R. Scipioni, D. Di Lecce, J. Hassoun, S. Dörfler, H. Altheus, S. Kaskel, C. Prehal, S. A. Freunberger, *J. Power Sources* **2020**, *480*, 228803.
[4] X. B. Cheng, R. Zhang, C. Z. Zhao, Q. Zhang, *Chem. Rev.* **2017**, *117*, 10403–10473.
[5] V. Marangon, C. Hernandez-Rentero, S. Levchenko, G. Bianchini, D. Spagnolo, A. Caballero, J. Morales, J. Hassoun, *ACS Appl. Energ. Mater.* **2020**, *3*, 12263–12275.
[6] G. Liu, Q. Sun, Q. Li, J. Zhang, J. Ming, *Energy Fuels* **2021**, *35*, 10405–10427.
[7] J. W. Fergus, *J. Power Sources* **2010**, *195*, 4554–4569.
[8] A. Manthiram, X. Yu, S. Wang, *Nat. Rev. Mater.* **2017**, *2*, 1–16.
[9] Q. Zhao, X. Liu, S. Stalin, K. Khan, L. A. Archer, *Nat. Energy* **2019**, *4*, 365–373.
[10] C. Wang, K. Fu, S. P. Kammampata, D. W. McOwen, A. J. Samson, L. Zhang, G. T. Hitz, A. M. Nolan, E. D. Wachsman, Y. Mo, V. Thangadurai, L. Hu, *Chem. Rev.* **2020**, *120*, 4257–4300.
[11] Y. Inaguma, L. Chen, M. Itoh, T. Nakamura, *Solid State Ionics* **1994**, *70–71*, 196–202.
[12] N. Anantharamulu, K. Koteswara Rao, G. Rambabu, B. Vijaya Kumar, V. Radha, M. Vithal, *J. Mater. Sci.* **2011**, *46*, 2821–2837.
[13] Z. Jian, Y. S. Hu, X. Ji, W. Chen, *Adv. Mater.* **2017**, *29*, 1601925.
[14] I. D. Seymour, E. Quérel, R. H. Brugge, F. M. Pesci, A. Aguadero, *ChemSusChem* **2023**, DOI 10.1002/cssc.202202215.
[15] D. Campanella, D. Belanger, A. Paolella, *J. Power Sources* **2021**, *482*, 228949.
[16] P. Molaiyan, S. E. Mailhiot, K. Voges, A. M. Kantola, T. Hu, P. Michalowski, A. Kwade, V. V. Telkki, U. Lassi, *Mater. Des.* **2023**, *227*, 111690.
[17] J. Li, K. Zhu, Z. Yao, G. Qian, J. Zhang, K. Yan, J. Wang, *Ionics* **2020**, *26*, 1101–1108.
[18] Z. Wan, D. Lei, W. Yang, C. Liu, K. Shi, X. Hao, L. Shen, W. Lv, B. Li, Q. H. Yang, F. Kang, Y. B. He, *Adv. Funct. Mater.* **2019**, *29*, 1–10.
[19] F. Han, Y. Zhu, X. He, Y. Mo, C. Wang, *Adv. Energy Mater.* **2016**, *6*, 1501590.
[20] H. Cavers, P. Molaiyan, M. Abdollahifar, U. Lassi, A. Kwade, *Adv. Energy Mater.* **2022**, *12*, 2200147.
[21] P. Gorai, T. Famprikis, B. Singh, V. Stevanović, P. Canepa, *Chem. Mater.* **2021**, *33*, 7484–7498.
[22] D. Bedrov, O. Borodin, J. B. Hooper, *J. Phys. Chem. C* **2017**, *121*, 16098–16109.
[23] X. Wang, Z. Sun, Y. Zhao, J. Li, Y. Zhang, Z. Zhang, *J. Solid State Electrochem.* **2020**, *24*, 111–119.
[24] S. Abouali, C.-H. Yim, A. Merati, Y. Abu-Lebdeh, V. Thangadurai, *ACS Energy Lett.* **2021**, *6*, 1920–1941.
[25] V. Thangadurai, S. Narayanan, D. Pinzaru, *Chem. Soc. Rev.* **2014**, *43*, 4714.
[26] M. Golozar, A. Paolella, H. Demers, S. Savoie, G. Girard, N. Delaporte, R. Gauvin, A. Guerfi, H. Lorrmann, K. Zaghib, *Sci. Rep.* **2020**, *10*, 1–11.
[27] V. Thangadurai, H. Kaack, W. J. F. Weppner, *J. Am. Ceram. Soc.* **2003**, *86*, 437–440.
[28] V. Thangadurai, W. Weppner, *J. Am. Ceram. Soc.* **2005**, *88*, 411–418.
[29] V. Thangadurai, W. Weppner, *Adv. Funct. Mater.* **2005**, *15*, 107–112.
[30] R. Murugan, V. Thangadurai, W. Weppner, *Angew. Chem. Int. Ed.* **2007**, *46*, 7778–7781.
[31] V. Thangadurai, W. Weppner, *J. Power Sources* **2005**, *142*, 339–344.
[32] N. Bernstein, M. D. Johannes, K. Hoang, *Phys. Rev. Lett.* **2012**, *109*, 205702.
[33] F. Chen, J. Li, Z. Huang, Y. Yang, Q. Shen, L. Zhang, *J. Phys. Chem. C* **2018**, *122*, 1963–1972.

[34] A. Paolella, W. Zhu, G. Bertoni, S. Savoie, Z. Feng, H. Demers, V. Gariepy, G. Girard, E. Rivard, N. Delaporte, A. Guerfi, H. Lorrmann, C. George, K. Zaghib, *ACS Appl. Energ. Mater.* **2020**, *3*, 3415–3424.
[35] J. Awaka, N. Kijima, H. Hayakawa, J. Akimoto, *J. Solid State Chem.* **2009**, *182*, 2046–2052.
[36] H. Buschmann, J. Dölle, S. Berendts, A. Kuhn, P. Bottke, M. Wilkening, P. Heitjans, A. Senyshyn, H. Ehrenberg, A. Lotnyk, V. Duppel, L. Kienle, J. Janek, *Phys. Chem. Chem. Phys.* **2011**, *13*, 19378–19392.
[37] S. Cao, S. Song, X. Xiang, Q. Hu, C. Zhang, Z. Xia, Y. Xu, W. Zha, J. Li, P. M. Gonzale, Y.-H. Han, F. Chen, *J. Korean Ceram. Soc.* **2019**, *56*, 111–129.
[38] C. A. Geiger, E. Alekseev, B. Lazic, M. Fisch, T. Armbruster, R. Langner, M. Fechtelkord, N. Kim, T. Pettke, W. Weppner, *Inorg. Chem.* **2011**, *50*, 1089–1097.
[39] J. Wolfenstine, J. Ratchford, E. Rangasamy, J. Sakamoto, J. L. Allen, *Mater. Chem. Phys.* **2012**, *134*, 571–575.
[40] C. Deviannapoorani, L. S. Shankar, S. Ramakumar, R. Murugan, *Ionics* **2016**, *22*, 1281–1289.
[41] J. F. Wu, E. Y. Chen, Y. Yu, L. Liu, Y. Wu, W. K. Pang, V. K. Peterson, X. Guo, *ACS Appl. Mater. Interfaces* **2017**, *9*, 1542–1552.
[42] A. Logéat, T. Köhler, U. Eisele, B. Stiaszny, A. Harzer, M. Tovar, A. Senyshyn, H. Ehrenberg, B. Kozinsky, *Solid State Ionics* **2012**, *206*, 33–38.
[43] K. Ishiguro, Y. Nakata, M. Matsui, I. Uechi, Y. Takeda, O. Yamamoto, N. Imanishi, *J. Electrochem. Soc.* **2013**, *160*, A1690–A1693.
[44] D. K. Schwanz, A. Villa, M. Balasubramanian, B. Helfrecht, E. E. Marinero, *AIP Adv.* **2020**, *10*, 035204.
[45] D. Campanella, S. Krachkovskiy, G. Bertoni, G. C. Gazzadi, M. Golozar, S. Kaboli, S. Savoie, G. Girard, A. C. Gheorghe Nita, K. Okhotnikov, Z. Feng, A. Guerfi, A. Vijh, R. Gauvin, D. Bélanger, A. Paolella, *J. Mater. Chem. A* **2023**, *11*, 364–373.
[46] Y. Li, Z. Wang, Y. Cao, F. Du, C. Chen, Z. Cui, X. Guo, *Electrochim. Acta* **2015**, *180*, 37–42.
[47] Y. Zeng, B. Ouyang, J. Liu, Y. Byeon, Z. Cai, L. J. Miara, Y. Wang, G. Ceder, *Science* **2022**, *378*, 1320–1324.
[48] S.-K. Jung, H. Gwon, H. Kim, G. Yoon, D. Shin, J. Hong, C. Jung, J.-S. Kim, *Nat. Commun.* **2022**, *13*, 7638.
[49] C. Deviannapoorani, L. Dhivya, S. Ramakumar, R. Murugan, *J. Power Sources* **2013**, *240*, 18–25.
[50] D. Wang, G. Zhong, O. Dolotko, Y. Li, M. J. McDonald, J. Mi, R. Fu, Y. Yang, *J. Mater. Chem. A* **2014**, *2*, 20271–20279.
[51] A. V. Virkar, T. D. Ketcham, R. S. Gordon, *Ceramurgia Int.* **1979**, *5*, 66–69.
[52] I. N. David, T. Thompson, J. Wolfenstine, J. L. Allen, J. Sakamoto, *J. Am. Ceram. Soc.* **2015**, *98*, 1209–1214.
[53] D. Campanella, G. Bertoni, W. Zhu, M. Trudeau, G. Girard, S. Savoie, D. Clément, A. Guerfi, A. Vijh, C. George, D. Bélanger, A. Paolella, *Chem. Eng. J.* **2023**, *457*, 141349.
[54] H. El-Shinawi, G. W. Paterson, D. A. MacLaren, E. J. Cussen, S. A. Corr, *J. Mater. Chem. A* **2017**, *5*, 319–329.
[55] L. Zhuang, X. Huang, Y. Lu, J. Tang, Y. Zhou, X. Ao, Y. Yang, B. Tian, *Ceram. Int.* **2021**, *47*, 22768–22775.
[56] H. El Shinawi, J. Janek, *J. Power Sources* **2013**, *225*, 13–19.

Manuscript received: March 19, 2023
Revised manuscript received: May 12, 2023
Accepted manuscript online: May 12, 2023
Version of record online: May 12, 2023